

# **Optimizing the homogenization technique for graphene nanoplatelet/yttria tetragonal zirconia composites: influence on the microstructure and the electrical conductivity**

C. López-Pernía<sup>1,2</sup>, C. Muñoz-Ferreiro<sup>2</sup>, C. González-Orellana<sup>2</sup>, A. Morales-Rodríguez<sup>2</sup>,  
Á. Gallardo-López<sup>2</sup>, R. Poyato<sup>1,2</sup>.

1. *Inst. Ciencia de Materiales de Sevilla, ICMS, CSIC-Universidad de Sevilla. Américo Vespucio 49. 41092 Sevilla. Spain.*

2. *Dpto. de Física de la Materia Condensada. ICMS, CSIC-Universidad de Sevilla. Apdo. 1065. 41080 Sevilla. Spain.*

## ***Abstract***

3 mol% yttria tetragonal zirconia polycrystalline (3YTZP) ceramic composite powders with 10 vol% nominal content of graphene nanoplatelets (GNPs) were prepared using four different homogenization routines: dispersion of the powder mixture by ultrasonication in isopropyl alcohol, homogenization in a high-energy planetary ball mill in wet or dry conditions after ultrasonication and milling of the powders in a high energy planetary ball mill in dry conditions. A significant effect of the homogenization routine on the powders particle size distribution was revealed by laser granulometry and Raman spectroscopy. Highly densified composites were obtained after spark plasma sintering (SPS) and remarkable differences on the GNP size, shape and distribution throughout the ceramic matrix and also in the electrical conductivity were observed in the four different composites. The composite with the best performance in terms of electrical conductivity was the one prepared after planetary ball milling of the powders in dry conditions as a consequence of the reduced dimensions of the GNPs and their excellent distribution throughout the ceramic matrix.

**Keywords:** composite materials, powder processing, microstructure, electrical conductivity

## **Introduction.**

The extraordinary and unprecedented properties of graphene have promoted a continuous growth of research activity in the last few years, reflected in an increasing number of patents and publications in different areas of science and technology. Among the different research areas in which graphene is being investigated, the investigation on graphene reinforced ceramics appears as a noteworthy field owing to the relevant properties that this bidimensional nanostructure imparts to ceramics. Together with the potential of producing tough composites by the incorporation of graphene to the ceramic structure, the obtaining of electrically conductive ceramic composites would allow the incorporation of these materials both in structural and multifunctional applications [1-3].

In the field of ceramic matrix composites, graphene-based nanomaterials (GBNs) as multilayer graphene (MLG) or graphene nanoplatelets (GNPs) are usually incorporated as a second phase. These nanomaterials, formed by the stacking of less than 10 graphene sheets for MLG and from 10 to 100 layers for GNPs, appear as a less expensive alternative to monolayer graphene while also exhibiting remarkable properties [4,5]. The incorporation of these GBNs into ceramic matrix composites has promoted improved mechanical [6,7] and electrical properties [8,9], as well as enhanced biocompatibility [10,11]. In particular, the enhancement in fracture toughness and wear resistance [12,13] are key issues for the implementation of these materials in biomedical applications as ceramic-on-ceramic hip implants with increased lifetimes and reduced events of catastrophic failure [14].

The potential of the graphene family in the field of ceramic composite materials will only be fully achieved when these GBN are homogeneously distributed into the ceramic matrices. However, this point has been noted as a critical factor, especially for composites with high contents of GNPs, as a result of the great tendency of graphene to form clusters or agglomerates through Van der Waals interactions [15]. Thus, the suitable mixing of the graphene-based material with the ceramic powder prior to sintering in order to achieve a homogeneous dispersion of the GNPs in the ceramic matrix is a critical issue since it directly affects the properties of the composite [1-3].

Several processing approaches have been proposed in the literature in order to deal with the GNP-ceramic powder critical mixing step [1-23]. Wet powder mixing using isopropyl alcohol or organic solvents, including ultrasonic agitation of the GNP suspension or of

the mixture with ceramic powder, is one of the most used techniques [16-18]. In some cases, magnetic stirring of the slurry [19,20] is also used, as well as attrition or ball milling using alcohol or organic solvents as liquid medium [21-24]. However, these techniques have been shown to apply a low energy during the powder homogenization, not enough to achieve agglomerate-free composites when high contents of GNPs are incorporated to the ceramic matrix [20,25]. On the other hand, it has been reported that the high-energy ball milling process can decrease the number of agglomerates in a more effective way than ultrasonic agitation or conventional milling, as it is a suitable technique not only to disperse, but also to reduce the number of graphene layers by exfoliating the GNPs and to decrease the lateral dimensions of the graphene nanoplatelets [3,25,26].

Recently, different authors have included high-energy ball milling in planetary mill as a homogenization step in the composite powder processing routine. The most common approach is to disperse the GNPs by ultrasonic agitation in alcohol or surfactants as liquid medium, and in a second step to homogenize the mixture of GNPs and ceramic powder in the planetary ball mill [7,27-29]. In other works, the high-energy ball milling was applied to the suspension of GNPs in alcohol [26] to subsequently mix them with the ceramic powder under ultrasonication, or both GNPs and ceramic powders were milled in dry conditions [30]. However, the studies reporting a systematic analysis of the effects of the powder homogenization treatment on the microstructure or properties of ceramic matrix composites are scarce [25, 31].

Michalkova et al [25] investigated the homogenization of a  $\text{Si}_3\text{N}_4/7$  wt% GNPs mixture using various milling techniques (attritor milling, ball milling and planetary ball milling) and their influence on the microstructure and on the fracture behaviour of silicon nitride-based composites prepared by hot press sintering. The fractographic analysis showed that agglomeration of the GNPs was the most common processing flaw, with agglomerate size from 20 to 400  $\mu\text{m}$  depending on the homogenization technique. The ultrasonicated planetary ball milled sample contained the smallest agglomerates and presented the best bending strength results among all the composites in the study.

Klimczyk et al [31] compared the homogenization of GNPs in  $\text{Si}_3\text{N}_4$  powders by planetary ball milling using various milling times, wetting mediums and rotation speeds and studied the effects on the microstructure and the mechanical properties of spark plasma sintered silicon nitride-based composites with 0.5, 1 and 2 wt% GNPs of three different grades. The microstructure of the composites depended remarkably on the milling duration, with

optimum results in terms of homogenization for 4-8 h milling time and 200 rpm rotation speed. A longer homogenization time caused a stronger fragmentation of the graphene flakes but did not entail an increase of the Young's modulus of the composites.

To date, most of the studies about composites with yttria stabilized zirconia matrix and graphene nanoplatelets have mainly focused on their microstructural and mechanical characterization, achieving enhanced values of hardness and fracture toughness for GNP contents up to 3 wt% [7,18,27,28,30]. The scarce works including electrical characterization of these composites have also reported a significant improvement in the electrical conductivity [9,20,30,32]. Nevertheless, the study of the effects of the powder homogenization technique on the electrical properties of the composites remains unexplored. The achievement of an optimized GNP distribution in the ceramic matrix through the use of suitable homogenization techniques would have a remarkable impact on the composite electrical conductivity. On the one hand, when GNP clustering takes place the real amount of GNPs dispersed in the ceramic grain boundaries is lower than the nominal content. Thus, achieving an agglomerate-free microstructure results in an optimized GNP percolation network. On the other hand, the possible fragmentation and exfoliation of the GNPs after high-energy ball milling [3,31] would result on an increased composite conductivity, as it has been reported that the GNP electrical conductivity increases with decreasing thickness [33,34].

In this study, we have used four different homogenization routines to prepare 3YTZP/GNP powders with a high amount of GNPs (10 vol%) with the objective of analyzing the effects of each of them in terms of the GNP size and distribution through the ceramic matrix on the 3YTZP based composites prepared by spark plasma sintering. The homogenization routines include the dispersion of the GNPs and the ceramic powder by ultrasonication in isopropyl alcohol, the homogenization in a high-energy planetary mill in wet or dry conditions after ultrasonication, and the milling of the powders in a high-energy planetary mill in dry conditions. The effect of each routine on the composite microstructure and electrical conductivity at room temperature has been analyzed.

## **2. Experimental procedure.**

### **2.1. Composite powders processing and characterization.**

GNPs with  $\leq 5 \mu\text{m}$  planar diameter and 50–100 nm thickness (Angstrom Materials, Dayton, Ohio, USA) and 3YTZP ceramic powder with 40 nm particle size (Tosoh Corporation, Tokyo, Japan) were used as the starting materials for the preparation of the composites. In order to elucidate the optimum homogenization technique for the preparation of the composite powders, the following routines were used:

**UA:** a dispersion of the GNPs in isopropyl alcohol was subjected to ultrasonic agitation for 15 min by means of an ultrasonic probe (Model KT-600, Kontes Inc., Vineland, NJ, USA) at 20 kHz and 95% amplitude, in time intervals of 5 min to avoid heating of the suspension to over 30 °C. The 3YTZP powder was added to the GNP suspension and sonicated for 5 min in order to homogenize the mixture. After drying on a hot plate with continuous magnetic stirring, the composite powders were homogenized in an agatha mortar.

**UA-W-PBM:** the GNPs and the 3YTZP powder were dispersed in isopropanol by ultrasonic agitation, as in the routine "UA". The slurry was dried in a rotary evaporator. Later, a suspension of the powder in isopropanol was homogenized in a planetary ball mill (PBM, Pulverisette 7, Fritsch, Germany) in wet conditions, at a speed of 350 rpm for 4 h. A relatively short milling time was chosen in order to avoid excessive fragmentation and damage of the GNPs [31]. The milling media consisted of 7 zirconia balls ( $d = 15 \text{ mm}$ ) in a 45 ml zirconia vial. The slurry was dried in a rotary evaporator and the powders were homogenized in an agatha mortar.

**UA-D-PBM:** the GNPs and the 3YTZP powder were dispersed in isopropanol by ultrasonic agitation, as in the routine "UA". The slurry was dried in a rotary evaporator. Later, the powders were homogenized in the planetary ball mill in dry conditions, at a speed of 350 rpm for 4 h.

**D-PBM:** the GNPs and the 3YTZP powder were homogenized in the planetary ball mill in dry conditions, at a speed of 350 rpm for 4 h.

In all the homogenization techniques, the use of surfactants that could introduce undesirable impurities as a consequence of incomplete surfactant removal was avoided.

The total C content (and consequently, the GNP content) in the composite powders was evaluated by elemental microanalysis (Elemental Analyzer TruSpec micro LECO) prior to sintering in order to establish possible GNPs or ceramic powders losses during processing. Approximately 1–3 mg of the composite powder were placed in Sn capsules

and completely burned in a pure oxygen environment at temperatures between 100 and 1000 °C. The combustion product (CO<sub>2</sub>) was quantified by an infrared cell. This study was performed at Microanalysis General Service (Centro de Investigación, Tecnología e Innovación de la Universidad de Sevilla, CITIUS).

The particle size distributions of the powders after the different homogenization routines were quantified using a laser particle size analyzer (Mastersizer 2000, Malvern, UK), using isopropyl alcohol as the liquid medium. The data were collected performing 5 scans of 12 s each scan. The Fraunhofer's model, which assumes spherical shape for the particles in suspension, was used. Thus, the obtained size distributions are not precise estimations of particle sizes and the results of the study must be considered as a comparison of the different prepared materials in suspension. Similar approaches to evaluate the graphene-based materials' particle size distributions have been previously proposed in the literature [35,36]. The study was performed at Functional Characterization Service (CITIUS).

Raman spectroscopy was used to assess the effects of the different powder processing routines on the structure and dimensions of the GNPs. The spectra were obtained using a dispersive microscope (Horiba Jobin Yvon LabRam HR800, Kyoto, Japan) equipped with a He-Ne green laser (532.14 nm) at 20 mW (Instituto de Ciencia de Materiales de Sevilla, ICMS). The microscope used a 100x objective and a confocal pinhole of 100 µm. The Raman spectrometer was calibrated using a silicon wafer. Six to eight spectra were taken for each sample.

## **2.2. Sintering and characterization.**

The composite powders were sintered by SPS (Model 515S, SPS Dr Sinter Inc., Kanagawa, Japan, CITIUS) at 1250 °C for 5 min with an applied uniaxial pressure of 75 MPa. The temperature was measured by means of an optical pyrometer focused on the side of the graphite die. The as-sintered composites had a diameter of ~15 mm and a thickness of ~2 mm. The surface graphite from the SPS moulding system was manually eliminated by grinding.

The density of the composites was measured with the Archimedes method using distilled water as the immersion medium. The theoretical density of the different composites was calculated using the rule of mixtures, considering  $\rho=6.05 \text{ g cm}^{-3}$  for 3YTZP and  $\rho=2.2 \text{ g}$

cm<sup>-3</sup> for GNPs (data from the suppliers), using the measured real GNP content in each case.

The presence and structural integrity of the GNPs in the composites after the sintering process were assessed by Raman spectroscopy on the fractured surfaces of the composites. Six to eight spectra from each specimen were acquired. The crystallographic phase identification was carried out using X-ray diffraction (XRD, model D8 Advance A25, Bruker Co., Massachusetts, USA, CITIUS). The microstructural observations of the sintered composites were carried out by high resolution scanning electron microscopy (HRSEM), using a Hitachi S5200 microscope (Hitachi High Technologies America Inc., USA) with the aim to analyze the distribution of the GNPs in the matrix and to characterize the ceramic grains morphology. The distribution and morphology of the GNPs in the composites were characterized by low magnification conventional SEM (FEI-Teneo, FEI, USA). Cross-section (c.s.) and inplane (i.p.) surfaces, i.e. surfaces parallel and perpendicular to the SPS pressing axis, were polished with diamond paste up to 1 μm for morphological studies. Polished c.s. surfaces devoted to characterize the ceramic grains were thermally treated in air at 1150 °C for 20 min to reveal the grain boundaries. The microstructural characterization was made by measuring approximately 300 grains/nanoplatelets for each sample. The ceramic grain size was estimated as the equivalent planar diameter,  $d = 2(\text{area}/\pi)^{1/2}$ . The GNPs morphology characterization was made by measuring the axial dimension (major diameter, D, and minor diameter, d) and the aspect ratio, A.R. = D/d, as size and shape parameters, due to their characteristic elongated shape.

The electrical conductivity was estimated using the capacitive method (metallization of two faces of the sample and measurement between the two electrodes). The measurements were performed on parallelepipedic specimens at room temperature by impedance spectroscopy using an Agilent 4294A analyzer in the frequency range 100 Hz - 2 MHz. A colloidal silver paste was applied on both sides of the samples and the electrodes were fired at 600 °C for 30 min under argon flow to avoid possible degradation of the GNPs during the process. Two different electrode configurations were used with the aim to acquire electrical conductivity in the directions parallel (□□) and perpendicular (□) to the SPS pressing axis, in order to account for any degree of electrical anisotropy.

### **3. Results and discussion.**

### 3.1. Characterization of the composite powders.

The results from the elemental microanalysis (Table 1) revealed that only small modifications of the GNP content with respect to the nominal one took place during the composite powder processing.

A remarkable effect of the homogenization routine is observed on the size distribution curves of the composite powders (Figure 1). For the powder prepared by application of ultrasonication in isopropyl alcohol a bimodal size distribution exhibiting two maxima at  $\sim 2$  and  $10 \mu\text{m}$ , with a higher particle volume % for the latter size, is observed. The second peak corresponds to a particle size higher than the specified data from the supplier ( $d_{\text{planar}} \leq 5 \mu\text{m}$ ), so it could be related to GNP clusters or agglomerates. When incorporating the PBM in wet conditions to the homogenization routine (UA-W-PBM), the shape of the size distribution curve is similar, but in this case the maxima are displaced to lower values, situated at  $\sim 1$  and  $4 \mu\text{m}$ , so a decrease of the particle size is promoted by the high-energy milling. However, this effect is not as significant as the observed one when the homogenization by milling in dry conditions is introduced in the powders processing routine (UA-D-PBM and D-PBM). Although a small peak in the size distribution curves is observed at  $\sim 20 \mu\text{m}$ , the main peak is situated at  $\sim 3 \mu\text{m}$  and a third peak at  $\sim 0.3 \mu\text{m}$  is also observed, revealing that most particles have a  $\leq 3 \mu\text{m}$  size. Moreover, narrower peaks at  $\sim 0.3$  and  $3 \mu\text{m}$  with a higher volume % of these particle classes are observed for the sample D-PBM. For this powder suspension, almost all the particles are smaller than  $3 \mu\text{m}$  and a non-negligible amount of them are smaller than  $0.3 \mu\text{m}$ . We can conclude that the homogenization of the GNP/ceramic powder mixture in a high-energy planetary mill in dry conditions not only can break the GNP agglomerates, but also promotes the fragmentation of the GNPs, in agreement with previously published studies [3,31].

The Raman spectra acquired on the composite powders prepared by the different homogenization routines are shown in Figure 2. The spectrum corresponding to the as received GNPs is included for comparison. The GNP characteristic D, G and 2D bands are observed for all the prepared powders, confirming the structural integrity of the GNPs after the different homogenization routines followed in this study.

Similar  $I_{\text{D}}/I_{\text{G}}$  values were obtained in the UA and UA-W-PBM powders when comparing with the as-received GNPs. The  $I_{\text{D}}/I_{\text{G}}$  ratio reflects the presence of crystal disorder or defects in graphitic materials. However, it is also related to the in-plane GNP size [37]



and it has been shown that the GNP borders are detected as defects by Raman spectroscopy as they present a strong D peak [19,38]. The absence of significant changes in the  $I_D/I_G$  ratio of the powders prepared by ultrasonic agitation and planetary ball mill in isopropanol reveals that these homogenization routines did not induce any structural modification or remarkable size decrease in the GNPs. On the contrary, the significant increase in the  $I_D/I_G$  ratio for the powders prepared by using the planetary ball mill in dry conditions confirms the decrease in the GNP size, previously indicated by the results obtained by laser granulometry (Figure 1). Nevertheless, the  $I_G/I_{2D}$  ratio and the 2D band shape in the spectra are very similar to the corresponding ones for graphite or for nanoplatelets with more than 10 graphene monolayers, so exfoliation has not taken place to produce  $n \leq 10$  graphene layers nanoplatelets [39].

### **3.2. Characterization of the sintered composites.**

#### **3.2.1. Density and microstructure.**

Highly densified composites were obtained for the four homogenization routines after SPS of the powders (Table 1). The density values are similar or even higher than reported densities for zirconia and yttria stabilized zirconia (YSZ) composites with lower GNP contents, also prepared using high-energy ball milling during powder composite processing and sintered by SPS [7,28] or by high-frequency induction-heated sintering [30]. These authors reported a decrease in density when increasing GNP content and maximum relative densities of 96% for  $ZrO_2/3$  wt% GNPs [30] and 98% for 3YTZP/1.5 wt% GNP and 5YSZ/2 vol% GNP [7,28].

The XRD patterns of the sintered composites are shown in Fig. 3. In all the composites the main phase is the reduced tetragonal zirconia ( $ZrO_{1.95}$ , JCPDS 01-081-1544). A minor contribution of the zirconia monoclinic phase (JCPDS 01-078-1807, main peaks at  $2\theta = 28.2$  and  $31.4^\circ$ ) [20] is observed in the composites with PBM homogenization.

The main graphite peak ( $2\theta = 26.6^\circ$ ) was also detected in two composites: UA and UAW-PBM.

The Raman spectra from the sintered composites, represented in Fig. 4, show D, G and 2D characteristic bands for the GNPs, confirming the absence of GNP structural deterioration after SPS process. The highest  $I_D/I_G$  ratios correspond to the composites prepared from powders homogenized in the PBM in dry conditions, which points to the

existence of GNPs with lower dimensions in these composites. However, there is a significant difference between the composites UA-D-PBM and D-PBM, with a much higher  $I_D/I_G$  ratio for the composite D-PBM. Although this fact could be related to a higher number of structural defects in the GNPs promoted during processing, it is more likely related to a more reduced planar dimension in the GNPs after the PBM in dry conditions. In this way, the presence of smaller GNPs homogeneously distributed throughout the matrix, with a higher exposure of the GNP edges in the fracture surface, would result in an increased D band.

Remarkable differences in the GNP size, shape and distribution in the ceramic matrix are revealed by the observations of the different composites fracture surfaces by HRSEM (Figures 5 and 6). The effect of the PBM performance on the microstructure of the composites prepared by homogenization routines including ultrasonic agitation is shown in Figure 5. When planetary ball milling is not included in the processing routine, the GNP planar dimensions are significantly larger than the ceramic grains, as previously shown [20]. A slight decrease of the GNP size is observed after including planetary ball milling in isopropyl alcohol, however, the most remarkable effect is observed in the composite prepared by planetary ball milling in dry conditions. In this composite, a remarkably smaller GNP size is observed, appearing in the same scale as the ceramic grains (Fig. 5(c)). In the microstructure of these three composites, prepared by processing routines including ultrasonic agitation, GNPs showing crumpling, bending and wavy surfaces can be observed, probably consequence of the high-energy applied by the ultrasonication probe. The figure 6 presents the microstructure of the composites prepared by planetary ball milling in dry conditions. These two composites present very similar microstructures with GNPs and 3YTZP grains with similar size. Nevertheless, the GNPs appearance is different, as the ones observed in the composite prepared without ultrasonication are mostly flat.

The GNP distribution in the ceramic matrix has been analysed by scanning electron microscopy using BSE imaging. In this mode, the 3YTZP matrix and the GNPs appear in the micrographs as light and dark phases, respectively. The figure 7 shows low magnification micrographs acquired in the polished c.s. surfaces of the studied composites. In the UA and UA-W-PBM composites, the GNPs appear preferentially aligned with their major surface perpendicular to the SPS compression axis (indicated by arrows), whereas they are randomly oriented in the in-plane surface (not shown). This structural anisotropy has been previously reported in several studies [16,20,22], also for

composites prepared from powders homogenized using planetary ball milling in wet conditions [25], and has been related to the uniaxial stress applied during sintering and to the high aspect ratio and stiffness of the GNPs. Large GNP-free ceramic areas with sizes ranging from 2 to 10  $\mu\text{m}$  can be observed among the GNPs in these two composites. On the contrary, the UA-D-PBM and D-PBM composites, prepared by planetary ball milling in dry conditions, exhibit a remarkably different distribution of the GNPs throughout the ceramic matrix. The GNPs present a smaller size and are homogeneously distributed in the matrix without any preferential alignment. Moreover, significantly smaller GNP-free ceramic areas can be found. In this case, no structural anisotropy was observed, as the microstructures observed in the i.p. surface (not shown) are similar to the ones observed in the c.s. one. Although the same uniaxial stress was applied during sintering of these composites and the composites UA and UA-W-PBM, in the former case the decreased GNP planar dimension after high-energy ball milling in dry conditions allows the GNPs to adapt easily to the grain contours and to be completely wrapping ceramic grains.

The distribution within the matrix and the aggregation of graphene or nanoparticles in polymer matrices with different volume fractions of nanomaterial has been previously described by dissipative particle dynamics (DPD) simulation [40,41]. Remarkable aggregation was described for the highest volume fractions of the nanomaterial, and different degrees of functionalization were stated in order to find what simulation parameter value would cause functionalized graphene to homogeneously disperse in the polymer matrix. In the present study, functionalization of the GNPs was avoided, and the homogeneous distribution of the nanomaterial was successfully achieved as a consequence of the smaller GNP size obtained after using the high-energy planetary ball mill in dry condition.

The table 2 displays the results of the GNP morphology characterization for all the composites. In agreement with the results of the laser granulometry study (Fig. 1), remarkable differences are observed between the GNP sizes in the composites. Although a decrease of the GNP size is promoted by the planetary ball milling in wet conditions with respect to the composite prepared from powders only subjected to ultrasonic agitation, significantly more reduced GNP dimensions are obtained after using the planetary ball milling in dry conditions in the powder processing routine, as it was pointed out by the Raman study (Fig. 4). It should be noted that both major and minor diameters,  $D$  (planar diameter) and  $d$  (thickness), are remarkably reduced so it is confirmed that the

dry PBM promotes both the fragmentation and the exfoliation of the GNPs. This size reduction explains the fact that the main graphite peak was not detected in the XRD patterns corresponding to these two composites, UA-D-PBM and D-PBM (Fig. 3). The aspect ratio of the GNPs is also modified by the use of PBM in dry conditions, with A.R.  $\sim 4$  for UA and UA-W-PBM composites and A.R.  $\sim 2$  for UA-D-PBM and D-PBM composites. The maximum major diameter for each composite has also been included in Table 2 in order to note that, although similar mean major and minor diameters have been obtained for UA-D-PBM and D-PBM composites, the smallest maximum D is achieved after planetary ball milling in dry conditions, so this homogenization routine is the one with the most remarkable effect in terms of reducing the GNP dimensions.

Regarding the matrix microstructure, a lower grain size was obtained in the composites prepared from the powders homogenized using planetary ball milling in dry conditions (UA-D-PBM and D-PBM, Table 1), despite having similar GNP content than the composites UA and UA-W-PBM (Table 1). Previous studies [20,26,30] have reported a decrease of ceramic grain size when increasing GNP content and have related this fact to the arrangement of the GNPs as diffusion barriers by wrapping around grains, which inhibits grain growth. At higher GNP content a higher number of ceramic grains becomes wrapped by GNPs, resulting in a grain refining effect. In the present study, the decreased GNP dimensions after the fragmentation and exfoliation promoted by the PBM in dry conditions (Table 2) results in an excellent distribution of the GNPs around the ceramic grains, which hinders grain coarsening during sintering. The narrower ceramic grain size distribution was obtained for the D-PBM composite (standard deviation  $0.07 \mu\text{m}$ , Table 1), revealing the optimized homogenizing effect on the matrix grain size of these processing conditions.

### 3.2.2. Electrical conductivity.

The electrical conductivities at room temperature in the directions parallel ( $\sigma_{\parallel}$ ) and perpendicular ( $\sigma_{\perp}$ ) to the SPS pressing axis are presented in Table 1. The composites UA and UA-W-PBM present electrical anisotropy with a higher conductivity in the direction perpendicular to the compression axis during SPS ( $\sigma_{\perp} > \sigma_{\parallel}$ ). The electrical anisotropy factors,  $\sigma_{\perp}/\sigma_{\parallel}$ , were found to be  $6.84 \pm 0.11$  and  $12.9 \pm 0.4$  for UA and UAW-PBM, respectively. The existence of electrical anisotropy in ceramic matrix composites with

GNPs has been previously reported by several authors [9,16,19,20] for composites with structural anisotropy consequence of a preferential alignment of the GNPs in the direction perpendicular to the compression axis during sintering, where the aligned GNPs present their major surface, as in the case of these two composites (Figure 4). This structural anisotropy and the intrinsic electrical anisotropy of graphene and graphene-related materials are the responsible factors for the observed electrical anisotropy. Despite the reduction of the GNP size in the UA-W-PBM composite (Table 2), an enhancement of the electrical conductivity is not achieved.

The two composites prepared from powders homogenized by PBM in dry conditions present higher conductivities in comparison with the composites UA and UA-W-PBM (Table 1) as a consequence of the excellent distribution of the GNPs in the ceramic matrix thanks to their reduced planar dimensions after the homogenization treatment (Table 2). Unlike composites UA and UA-W-PBM, the composites UA-D-PBM and D-PBM do not present remarkable electrical anisotropy. The electrical conductivities obtained in the directions perpendicular and parallel to the compression axis during SPS are quite similar, being slightly higher in the parallel direction. This is related to the lack of preferential alignment of the GNPs in these composites, as shown in the BSE-SEM images (Figure 7). The fact that the composite D-PBM shows higher conductivity than UA-D-PBM reveals that the GNPs were not damaged during the PBM in dry conditions, as could be inferred from the increased D Band in the Raman spectra from this composite (Figure 4). Thus, it is confirmed that the higher  $I_D/I_G$  ratio in this composite is a consequence of the smaller planar dimension of the GNPs.

It can be concluded that the composite with the best performance in terms of electrical conductivity is D-PBM. This is consequence of the reduced dimensions of the GNPs in this composite and their excellent distribution throughout the ceramic matrix. The different GNP appearance in this composite, with mostly flat GNPs whereas in the composite UA-D-PBM they present a wavy aspect (Fig. 6), could also have an influence on conductivity, however, further studies in order to clarify this fact are needed.

In summary, by selecting the appropriate homogenization technique it is possible to obtain composites with enhanced electrical conductivity and without remarkable anisotropy that would be excellent candidates for the application of the electro discharge machining technique (EDM) in order to manufacture miniaturized complex shapes from the

composites that could be used in applications such as micro-electro-mechanical systems (MEMS) [8,42].

#### **4. Conclusions.**

Highly densified yttria tetragonal zirconia composites with 10 vol% GNPs were fabricated by SPS from powders prepared by using four different homogenization techniques including ultrasonication in isopropyl alcohol and/or homogenization in a high-energy planetary ball mill in wet or dry conditions.

The remarkably different particle size distribution of the powders after using the different homogenization routines had a great impact on the composites microstructure and electrical conductivity. The bigger GNPs, preferentially oriented in the direction perpendicular to the SPS pressing axis, observed in the composites obtained after homogenization of the powders by ultrasonication or by high-energy planetary ball milling in isopropyl alcohol resulted in a remarkable electrical anisotropy, with higher conductivities in the direction where the aligned GNPs present their major surface. On the contrary, the significantly smaller GNP planar dimensions and thicknesses, obtained due to the fragmentation and exfoliation promoted during high-energy ball milling in dry conditions, allow the GNPs to adapt easily to the grain contours and to be completely wrapping the ceramic grains. This resulted in composites where the GNPs are homogeneously distributed thorough the ceramic matrix without any preferential alignment, i.e. without structural anisotropy, with a lower grain size and with an enhanced and isotropic electrical conductivity.

It can be concluded that the homogenization of the powder mixture by high-energy planetary ball milling in dry conditions without previous ultrasonication results in the composite with the best performance in terms of microstructural homogeneity and electrical conductivity.

#### **Acknowledgments.**

Financial support from project MAT2015-67889-P (Spanish Ministerio de Economía y Competitividad), cofunded by European FEDER funding, is acknowledged. Authors are

grateful to Prof. F.J. Gotor (ICMS) for providing access to the planetary ball mill and to Mr. J. Cáceres for showing that serendipity really happens.

## Figure Captions.

**Figure 1:** Particle size distribution, estimated by laser granulometry, of the 3YTZPGNP composite powders after the different homogenization techniques.

**Figure 2:** Raman spectra of the composite powders prepared by the different homogenization routines. The spectra were normalized to the G band for easier comparison. The  $I_D/I_G$  ratios are also indicated.

**Figure 3:** X- ray diffraction patterns of the 3YTZP-GNP composites sintered from the powders prepared by the different homogenization routines.

**Figure 4:** Raman spectra of the fracture surface of the 3YTZP-GNP composites sintered from the different powders. The spectra were normalized to the G band for easier comparison. The  $I_D/I_G$  ratios are also indicated.

**Figure 5:** Effect of the planetary ball milling conditions on the microstructure of the composites prepared by homogenization routines including ultrasonic agitation.

**Figure 6:** Effect of the ultrasonic probe on the microstructure of the composites prepared by planetary ball milling in dry conditions.

**Figure 7:** BSE-SEM images of the polished cross section surfaces of the composites prepared by the different homogenization routines. Compression axis during SPS is indicated in (b) by arrows.



## References

- 1 I. Ahmad, B. Yazdani, Y. Zhu, Recent advances on carbon nanotubes and graphene reinforced ceramics nanocomposites, *Nanomater.* 5 (2015) 90-114.
- 2 P. Miranzo, M. Belmonte, M. I. Osendi, From bulk to cellular structures: A review on ceramic/graphene filler composites, *J. Eur. Ceram. Soc.* 37 (2017) 3649–3672.
- 3 K. Markandan, J.K. Chin, M.T.T. Tan, Recent progress in graphene based ceramic composites: a review, *J. Mater. Res.* 32 (2017) 84-106.
- 4 A. Bianco et al, All in the graphene family – A recommended nomenclature for twodimensional carbon materials, *Carbon* 65 (2013) 1–6.
- 5 P. Wick et al, Classification framework for graphene-based materials, *Angew. Chem. Int. Ed.* (2014) 7714-7718.
- 6 C. Ramirez, P. Miranzo, M. Belmonte, M.I. Osendi, P. Poza, S.M. Vega-Diaz, M. Terrones, Extraordinary toughening enhancement and flexural strength in  $\text{Si}_3\text{N}_4$  composites using graphene sheets, *J. Eur. Ceram. Soc.* 34 (2014) 161–169.
- 7 J. Liu, H. Guo, Y. Su, L. Wang, L. Wei, G. Yang, Y. Yang, K. Jiang, Spark plasma sintering of graphene platelet reinforced zirconia composites with improved mechanical performance, *Mater. Sci. Eng. A* 688 (2017) 70–75.
- 8 F. Zeller, C. Müller, P. Miranzo, M. Belmonte, Exceptional micromachining performance of silicon carbide ceramics by adding graphene nanoplatelets, *J. Eur. Ceram. Soc.* 37 (2017) 3813–3821.
- 9 R. Poyato, J. Osuna, A. Morales-Rodríguez, Á. Gallardo-López, Electrical conduction mechanisms in graphene nanoplatelet/yttria tetragonal zirconia composites, *Ceram. Int.* (in press).
- 10 M. Mehrali, E. Moghaddam, S. F. S. Shirazi, S. Baradaran, M. Mehrali, S. T. Latibari, H. S. C. Metselaar, N. A. Kadri, K. Zandi, N. A. A. Osman, Synthesis, mechanical properties, and in vitro biocompatibility with osteoblasts of calcium silicate–reduced graphene oxide composites, *ACS Appl. Mater. Interf.* 6 (2014) 3947–3962.
- 11 C. Gao, P. Feng, S. Peng, C. Shuai, Carbon nanotube, graphene and boron nitride nanotube reinforced bioactive ceramics for bone repair, *Acta Biomater.* 61 (2017) 1–20.
- 12 M. Belmonte, C. Ramirez, J. Gonzalez-Julian, J. Schneider, P. Miranzo, M.I. Osendi, The beneficial effect of graphene nanofillers on the tribological performance of ceramics, *Carbon* 61 (2013) 431–435.

- 13 M. Maros B., A. K. Németh, Z. Károly, E. Bódis, Z. Maros, O. Tapasztó, K. Balázs, Tribological characterisation of silicon nitride/multilayer graphene nanocomposites produced by HIP and SPS technology, *Tribology Int.* 93 (2016) 269–281.
- 14 A. Nieto, J.M. Zhao, Y.-H. Han, K.H. Hwang, J.M. Schoenung, Microscale tribological behavior and in vitro biocompatibility of graphene nanoplatelet reinforced alumina, *J. Mech. Behavior Biomed. Mater.* 61 (2016) 122–134.
- 15 V. Singh, D. Joung, L. Zhai, S. Das, S.I. Khondaker, S. Seal, Graphene based materials: past, present and future, *Prog. Mater. Sci.* 56 (2011) 1178–1271.
- 16 C. Ramirez, F.M. Figueiredo, P. Miranzo, P. Poza, M.I. Osendi, Graphene nanoplatelet/silicon nitride composites with high electrical conductivity, *Carbon* 50 (2012) 3607–3615.
- 17 I.N.G. Simsek, A. Nistal, E. García, D. Pérez-Coll, P. Miranzo, M.I. Osendi, The effect of graphene nanoplatelets on the thermal and electrical properties of aluminum nitride ceramics, *J. Eur. Ceram. Soc.* 37 (2017) 3721–3729.
- 18 J. Su, Y. Chen, Q. Huang, Graphene nanosheet-induced toughening of yttrium-stabilized zirconia, *Appl. Phys. A* (2017) 123:10.
- 19 B. Román-Manso, E. Domingues, F.M. Figueiredo, M. Belmonte, P. Miranzo, Enhanced electrical conductivity of silicon carbide ceramics by addition of graphene nanoplatelets, *J. Eur. Ceram. Soc.* 35 (2015) 2723–2731.
- 20 A. Gallardo-López, I. Márquez-Abril, A. Morales-Rodríguez, A. Muñoz, R. Poyato, Dense graphene nanoplatelet/yttria tetragonal zirconia composites: processing, hardness and electrical conductivity, *Ceram. Int.* 43 (2017) 11743–11752.
- 21 P. Hvizdos, J. Dusza, C. Balázs, Tribological properties of Si<sub>3</sub>N<sub>4</sub>-graphene nanocomposites, *J. Eur. Ceram. Soc.* 33 (2013) 2359–2364.
- 22 O. Tapasztó, L. Tapasztó, H. Lemmel, V. Puchy, J. Dusza, C. Balázs, K. Balázs, High orientation degree of graphene nanoplatelets in silicon nitride composites prepared by spark plasma sintering, *Ceram. Int.* 42 (2016) 1002–1006.
- 23 Y. Tan, H. Zhang, S. Peng, Electrically conductive graphene nanoplatelet/boron carbide composites with high hardness and toughness, *Scripta Mater.* 114 (2016) 98–102.
- 24 Y. Celik, A. Celik, E. Flahaut, E. Suvaci, Anisotropic mechanical and functional properties of graphene-based alumina matrix nanocomposites, *J. Eur. Ceram. Soc.* 36 (2016) 2075–2086.

- 25 M. Micháľková, M. Kasiarová, P. Tatarko, J. Dusza, P. Sajgalík, Effect of homogenization treatment on the fracture behaviour of silicon nitride/graphene nanoplatelets composites, *J. Eur. Ceram. Soc.* 34 (2014) 3291–3299.
- 26 A. Nieto, L. Huang, Y.-H. Han, J.M. Schoenung, Sintering behavior of spark plasma sintered alumina with graphene nanoplatelet reinforcement, *Ceram. Int.* 41 (2015) 5926–5936.
- 27 D.-T. Vu, Y.-H. Han, F. Chen, D. Jin, J.M. Schoenung, D.-Y. Lee, Graphene nanoplatelets reinforced ZrO<sub>2</sub> consolidated by spark plasma sintering, *Science Adv. Mater.* 7 (2015) 1–6.
- 28 S. Li, Z. Xie, Y. Zhang, Y. Zhou, Enhanced toughness of zirconia ceramics with graphene platelets consolidated by spark plasma sintering, *Int. J. Appl. Ceram. Technol.* 14 (2017) 1062–1068.
- 29 S. Baskut, A. Cinar, S. Turan, Directional properties and microstructures of spark plasma sintered aluminum nitride containing graphene platelets, *J. Eur. Ceram. Soc.* 37 (2017) 3759–3772.
- 30 S.-M. Kwon, S.-J. Lee, I.-J. Shon, Enhanced properties of nanostructured ZrO<sub>2</sub>–graphene composites rapidly sintered via high-frequency induction heating, *Ceram. Int.* 41 (2015) 835–842.
- 31 P. Klimczyk, L. Jaworska, P. Putyra, Z. Pedzich, J. Laszkiewicz–Łukasik, Effect of milling parameters on microstructure and selected mechanical properties of Si<sub>3</sub>N<sub>4</sub> – graphene composites, *Key Eng. Mater.* 655 (2015) 17-21.
- 32 K. Markandan, J.K. Chin, M.T.T Tan, Enhancing electroconductivity of yttria stabilised zirconia ceramic using graphene platlets, *Key Eng. Mater.* 690 (2016) 1-5. 33
- P.N. Nirmalraj, T. Lutz, S. Kumar, G.S. Duesberg, J.J. Boland, Nanoscale mapping of electrical resistivity and connectivity in graphene strips and networks, *Nano Lett.* 11 (2011) 16–22.
- 34 X.-Y. Fang, X.-X. Yu, H.-M. Zheng, H.-B. Jin, L. Wang, M.-S. Cao, Temperature and thickness-dependent electrical conductivity of few-layer graphene and graphene nanosheets, *Phys. Lett. A* 379 (2015) 2245–2251.

- 35 A.M. Pinto, C. Gonçalves, D.M. Sousa, A.R. Ferreira, J. Agostinho Moreira, I.C. Gonçalves, F.D. Magalhães, Smaller particle size and higher oxidation improves biocompatibility of graphene-based materials. *Carbon* 99 (2016) 318-329.
- 36 W.X. Li, Z.W. Xu, L. Chen, M.J. Shan, X. Tian, C.Y. Yang, et al., A facile method to produce graphene oxide-g-poly(L-lactic acid) as an promising reinforcement for PLLA nanocomposites, *Chem. Eng. J.* 237 (2014) 291-299.
- 37 L. G. Cançado, K. Takai, T. Enoki, M. Endo, Y. A. Kim, H. Mizusaki, A. Jorio, L. N. Coelho, R. Magalhães-Paniago, M. A. Pimenta, General equation for the determination of the crystallite size of nanographite by Raman spectroscopy, *Appl. Phys. Lett.* 88, 163106 (2006).
- 38 C. Casiraghi, A. Hartschuh, H. Qian, S. Piscanec, C. Georgi, A. Fasoli, K.S. Novoselov, D.M. Basko, A.C. Ferrari, Raman spectroscopy of graphene edges, *Nano Lett.* 9 (2009) 1433–1441.
- 39 A.C. Ferrari, J.C. Meyer, V. Scardaci, C. Casiraghi, M. Lazzeri, F. Mauri, S. Piscanec, D. Jiang, K.S. Novoselov, S. Roth, A.K. Geim, Raman spectrum of graphene and graphene layers, *Phys. Rev. Lett.* 97 (18) (2006) 187401.
- 40 H. Chen, E. Ruckenstein, Nanoparticle aggregation in the presence of a block copolymer, *J. Chem. Phys.* 131 (2009) 244904.
- 41 S.-P. Ju, Y.-C. Wang, G.-J. Huang, J.-W. Chang, Miscibility of graphene and poly(methyl methacrylate) (PMMA): molecular dynamics and dissipative particle dynamics simulations, *RSC Adv* 3 (2013) 8298–8307.
- 42 J.-W. Sung, K.-H. Kim, M.-C. Kang, Effects of graphene nanoplatelet contents on material and machining properties of GNP-dispersed Al<sub>2</sub>O<sub>3</sub> ceramics for micro-electric discharge machining, *Int. J. Precision Eng. Manufacturing-Green Technol.* 3 (2016) 247-252.

## \*Highlights

- High-energy planetary ball milling PBM in dry condition strongly reduces GNP's size
- 3YTZP/GNP composite after wet PBM has anisotropic structure/conductivity after SPS
- 3YTZP/GNP composites after dry PBM don't show structural anisotropy after SPS
- GNP dry PBM enhances the isotropic electrical conductivity of 3YTZP/GNP composites

**Table 1:** Measured GNP content, density, grain size and electrical conductivity for the GNP/3YTZP composites.

<b>Homogenization routine</b>	<b>Real GNP content (vol% )</b>	<b><math>\rho</math> (g/cm<sup>3</sup>)</b>	<b><math>\rho_{\text{relative}}</math> (%)</b>	<b>d (<math>\mu\text{m}</math>)</b>	<b>s.d. (<math>\mu\text{m}</math>)</b>	<b><math>\sigma_{\parallel}</math> (S·m<sup>-1</sup>)</b>	<b><math>\sigma_{\perp}</math> (S·m<sup>-1</sup>)</b>
<b>UA</b>	8.96±0.06	5.69±0.16	99.65±0.20	0.25*	0.11*	16.6 ± 0.11**	113.3 ± 1.1**
<b>UA-W-PBM</b>	8.93±0.06	5.61±0.06	98.4±1.1	0.30	0.12	6.07 ± 0.14	78.6 ± 0.5
<b>UA-D-PBM</b>	9.39±0.09	5.59±0.3	98.3±0.5	0.22	0.10	125.0 ± 0.9	127.1 ± 0.9
<b>D-PBM</b>	9.18±0.16	5.47±0.06	95.9±1.3	0.18	0.07	406 ± 3	471 ± 5

\*From Ref. [20]

\*\*From Ref. [9]

**Table 2:** Morphological parameters of the GNPs measured for each composite.

<b>Homogenization routine</b>	<b>D (<math>\mu\text{m}</math>)</b>	<b>s.d. (<math>\mu\text{m}</math>)</b>	<b>D<sub>max</sub> (<math>\mu\text{m}</math>)</b>	<b>d (<math>\mu\text{m}</math>)</b>	<b>s.d. (<math>\mu\text{m}</math>)</b>	<b>A.R.</b>	<b>s.d.</b>
<b>UA</b>	2.3	2.0	16.5	0.6	0.4	3.7	2.5
<b>UA-W-PBM</b>	1.5	1.5	12.1	0.35	0.21	4.3	2.7
<b>UA-D-PBM</b>	0.32	0.30	2.6	0.16	0.09	2.0	1.0
<b>D-PBM</b>	0.39	0.22	1.6	0.18	0.08	2.2	0.8

Figure 1

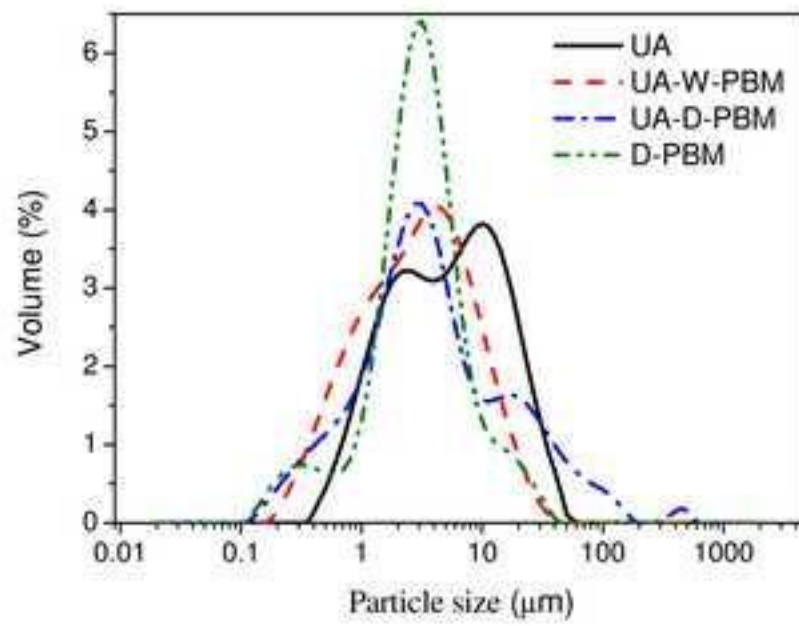




Figure 2

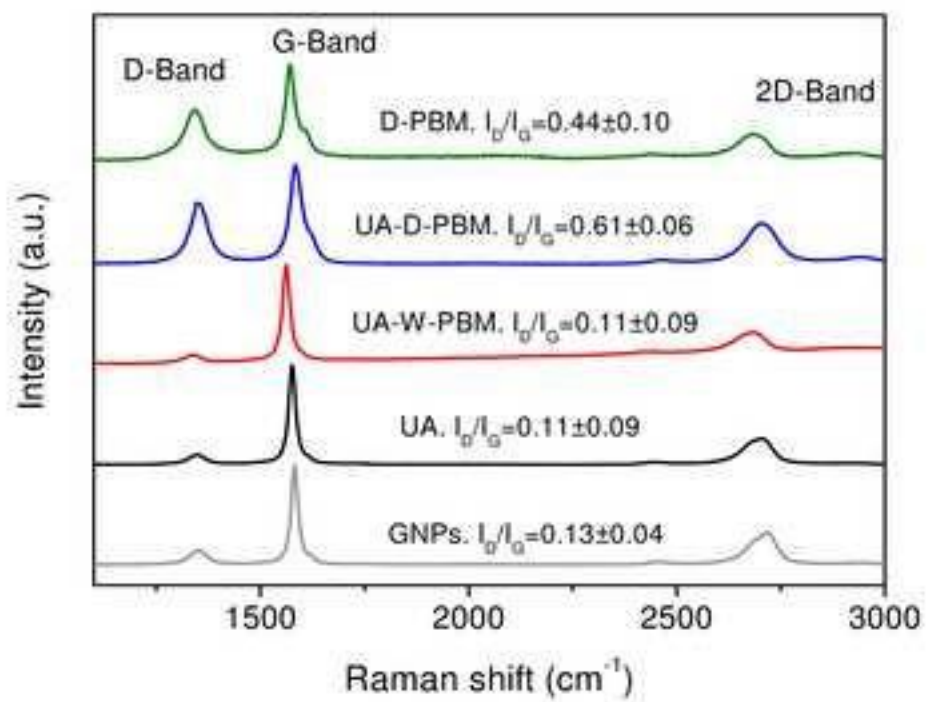


Figure 3

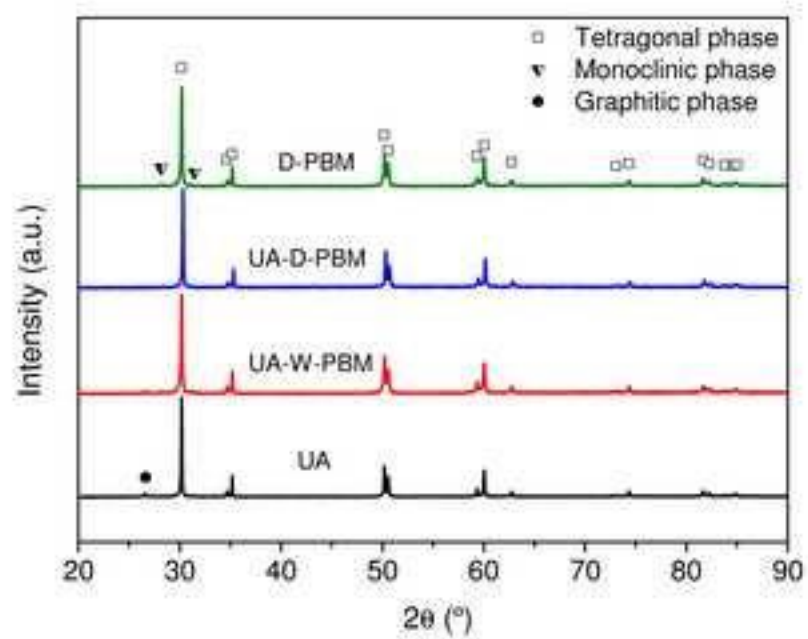


Figure 4

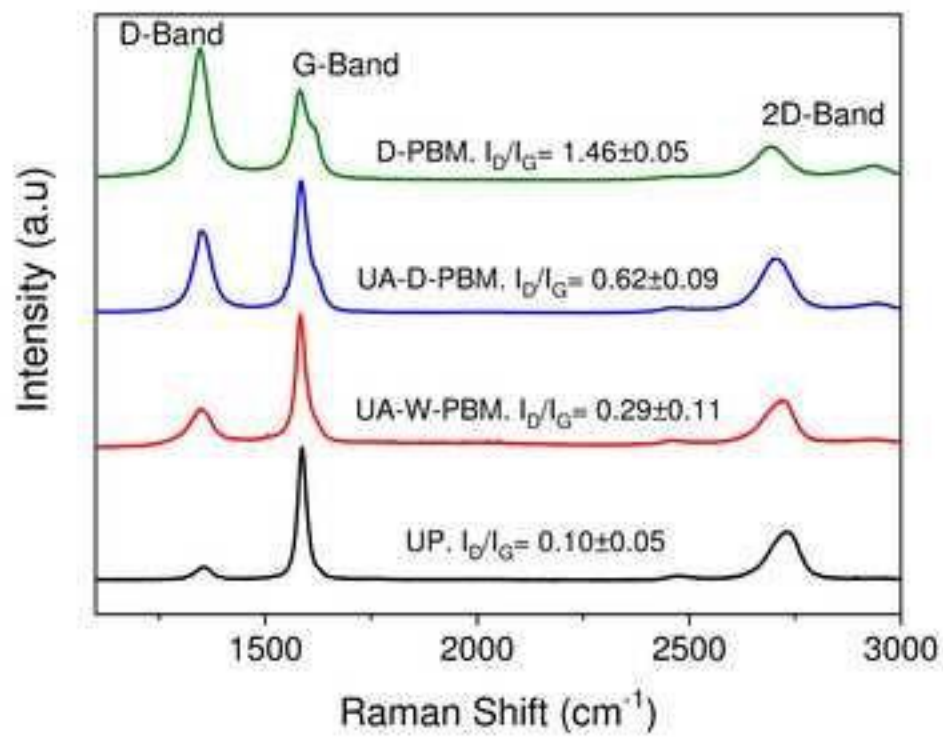


Figure 5

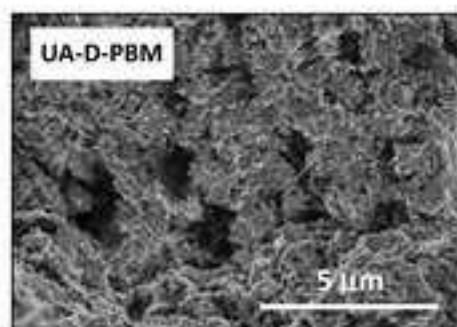
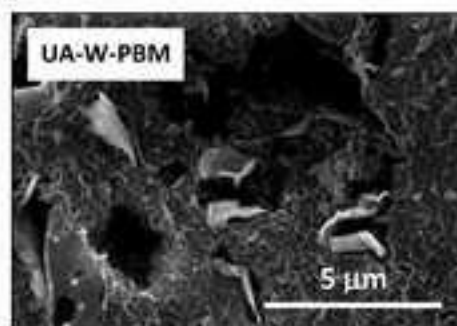
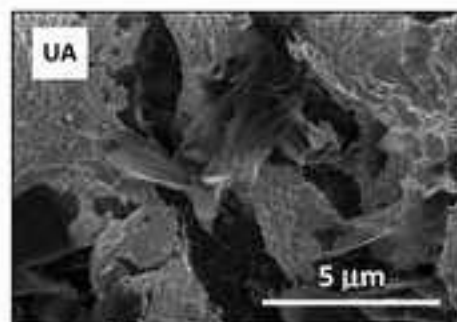


Figure 6

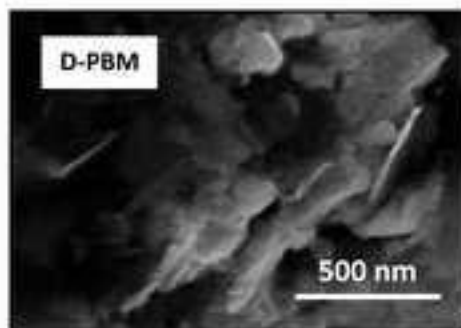
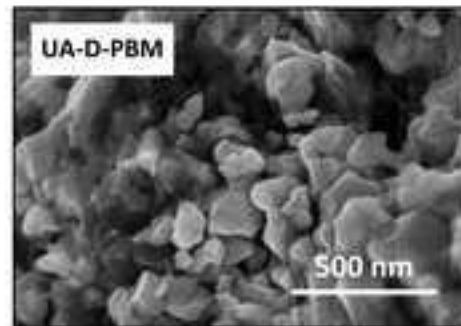


Figure 7

